Quantum dot-based FRET nanosensors for Talin-membrane assembly and mechanosensing

Audrey Ntadambanya [1], Julien Pernier [2], Violaine David [1], Kimihiro Susumu [3], Igor L. Medintz [3], Mayeul Collot [4], Andrey Klymchenko [4], Niko Hildebrandt [5], Isabelle Le Potier [6], Christophe Le Clainche [1], Marcelina Cardoso Dos Santos [1]*

[1] Université Paris-Saclay, CEA, CNRS, Institute for Integrative Biology of the Cell (I2BC), Gif-sur-Yvette, France
[2] Gustave Roussy Institute, Inserm U1279, Université Paris-Saclay, Villejuif, France
[3] Center for Bio/Molecular Science and Engineering U.S. Naval Research Laboratory Washington, USA
[4] Laboratoire de Bioimagerie et Pathologie, CNRS UMR 7021 Université de Strasbourg, Strasbourg, France
[5] Department of Engineering Physics, McMaster University, Hamilton, ON L8S4L7, Canada
[6] C2N, CNRS UMR9001, Université Paris-Saclay, Palaiseau, France.

*Corresponding author: marcelina.cardoso-dos-santos@i2bc.paris-saclay.fr

ABSTRACT. Understanding the mechanisms of assembly and disassembly of macromolecular structures in cells relies on solving biomolecular interactions. However, those interactions often remain unclear because tools to track molecular dynamics are not sufficiently resolved in time or space. In this study, we present a straightforward method for resolving inter- and intra-molecular interactions in cell adhesive machinery, using quantum dot (QD) based Förster resonance energy transfer (FRET) nanosensors. Using mechanosensitive protein Talin, one of the major components of focal adhesions, we are investigating mechanosensing ability of proteins to sense and respond to mechanical stimuli. First, we quantified the distances separating Talin and a giant unilamellar vesicle membrane for three Talin variants. These variants differ in molecular length. Second, we investigated the mechanosensing capabilities of Talin, i.e., its conformation changes due to mechanical stretching initiated by cytoskeleton contraction. Our results suggest that in early focal adhesion, Talin undergoes stretching, corresponding to a decrease in the Talin-membrane distance of 2.5 nm. We demonstrate that QD-FRET nanosensors can be applied for the sensitive quantification of mechanosensing with sub-nanometer accuracy.

KEYWORDS : Nanoparticles, nanosensors, fluorescence microscopy, Förster resonance energy transfer, cell adhesion, mechanosensing

Transmission of force between the cell and its environment is essential for the cell adhesion and migration required for tissue building and repair. Transmission of force across the cell plasma membrane is facilitated by focal adhesions (FAs), which are highly organised, self-assembled adhesive complexes [1], [2]. FAs form where force transfer between the cytoskeleton and the environment is required. Some of FA compounds, including Talin, are capable of sensing cytoskeletal tension [3], [4]. Talin is a large (270 kDa) intracellular protein consisting of a head domain (F_0-F_3), a flexible neck, and a tail of 13 rod subdomains (R_1-R_{13}). Its head domain binds to the cell plasma membrane. On the one hand, it interacts with inositol phosphate groups [5], [6] of phosphatidylinositol 4,5-bisphosphate (PIP_2) lipids at the plasma membrane, releasing Talin autoinhibition [7], [8]. Interestingly, it was demonstrated that F_3 interacts with R_9 and F_2 with R_{12}, resulting in an inactive snake like biting its own tail conformation [6], [9]. On the other hand, the transmembrane adhesion receptors Integrins are also known to disrupt the autoinhibition interaction in cells [10]. Talin's head activates Integrins and enhances cell attachment to the extracellular matrix [11]. The rod subdomains in Talin tail bind Actin which polymerizes in filaments. Myosin II, the molecular motor, grafts filaments and applies tension by contracting them [12]. Consequently, Talin's multiple helical bundle rod subdomains unfold, leading to the revelation of new protein binding sites [13], allowing maturation of FAs [4]. Therefore, Talin can interact with numerous other FA components and form macromolecular assemblies.

The mechanism of Talin unfolding, due to mechanosensing, is not fully understood. For example, the orderly unfolding of Talin as a result of Actin-Myosin stretching has never been revealed. Owing to the large size of Talin, resolving its unstretched conformation via

crystallography has not been accomplished either. Dedden et al. observed that Talin unfolds from a 15 nm globular arrangement to a 60 nm string-like structure via cryoelectron microscopy [9]. Using magnetic tweezers, it was possible to artificially unfold Talin into a stretched conformation of up to 250 nm [14]. However, that system did not account for the Talin-membrane interaction. Super-resolution microscopy on fixed cells reported Talin elongations of 180 nm [13] or even up to 350 nm [15]. Talin unfolding due to mechanosensing is therefore a topic of debate. Those examples show that better spatially and temporally resolved probes for tracking of molecular assemblies are required to understand how cells sense the force of the cytoskeleton.

To improve the comprehension of how Talin interacts with the plasma membrane and undergoes molecular stretching, intermolecular FRET nanosensors have been developed. FRET is a non-radiative energy transfer that occurs between an excited state donor and a ground state acceptor. It is widely applied for biosensing and analysis of biomolecular binding [16], [17]. Fluorescent protein (FP) based FRET biosensors have already demonstrated cytoskeleton-dependent stretching of Talin [18], [19]. However, the use of FP-based biosensors has limitations. It may require delicate bleed-through corrections, parallelization (one by one sensor), or multi-read out (spectral coupled with lifetime) and be prone to photobleaching [16], [17], [20]. Furthermore, the FRET pair must be inserted in a restricted distance region to sense cytoskeleton tension. Typically, donor and acceptor FPs are separated by a short linker between two structural regions [18] or delimit protein ends [15], [19]. Although highly sophisticated, these biosensors were unable to reveal the underlying process of Talin stretching. Certain studies have extracted FA protein conformations [21], but FRET with conventional fluorophores has limited the distance range to circa 2 to 9 nm [22]. When using QD-based FRET nanosensors, this distance range can be doubled and molecular distances can be quantified with a spatial resolution far below the optical diffraction limit [23]–[26]. The

spectrally broad absorption, large Stokes shift, and narrow emission of QDs are ideal for efficiently removing background signals that can be very problematic for FP-FRET biosensors. It is almost impossible to excite only the FP FRET donor. Acceptor background caused by direct light excitation, must be subtracted via control experiments of using the acceptor FP alone. Whereas FRET ratio (emission intensities of donor and acceptor) measurements can alleviate the problem, the FRET ratio does not readily provide quantitative distance information. In contrast, QD-FRET nanosensors only need to measure the photoluminescence intensity of the QD donor alone and in the presence of the acceptor to directly assess donor-acceptor distances.

In this study, we demonstrated that QD-FRET nanosensors can be applied for the quantification of biomolecular interactions of FA proteins such as Talin. We were able to measure the separation distances between Talin and a giant unilamellar vesicle (GUV) membrane with sub-nanometer precision. This allowed us to deduce how larger or smaller Talin variants associate with the membrane. In addition, our mechanosensing study showed that Actin-Myosin contraction produced shortening of the distance between the GUV membrane and Talin tail end, suggesting an elongation of the Talin parallel to the membrane. The *in vitro* model used in the study mimicked ventral Actin-Myosin stress fibers, which are located on the adhesion cell surface and contract between two successive FAs [27]. Indeed, ventral stress fibers play a fundamental role in cell retraction and shape changes during cell migration.

RESULTS AND DISCUSSION

Minimal focal adhesion autoassembles on GUV membrane. The biomimetic *in vitro* model used in our study reconstituted a minimal FA composed of Talin-1, a mechanosensing protein, and Actin and Myosin cytoskeleton proteins (Fig 1A). The interaction between Talin and the lipid bilayer was driven by PIP_2 lipids, which were embedded in the GUV membrane. Indeed, this protein-membrane interaction is required for Talin to undergo a conformational change, exposing new binding sites for transmembrane Integrins [7], [28], [29]. In addition, GUVs contained cholesterol to mimic the plasma membrane of FA, which is characterized by a high steroid content [30]. To investigate membrane associated biomolecular assembly, three variants of recombinant Talin were produced based on the rod subdomain structure. Each variant had a portion of the head domain responsible for PIP_2 binding (F_2-F_3 domains). However, the Talin variants differed in their Actin-binding ability and tail length (i.e., the number of rod subdomains, see Fig 1 B,C,D). The only one Actin binding variant, Actin binding Talin (AB-Ta, Fig 1B), was short and contained four rod subdomains (R_1-R_2-R_3-R_{13}), including R_{13} known for primarily binding Actin [31]. Indeed, it has been demonstrated via magnetic tweezers that pulling on R_{13} results in a response from the subdomains opposite to it, namely R_1-R_2-R_3 [14]. The second variant, delta Actin binding Talin (ΔAB-Ta), lacked R_{13} and was unable to interact with Actin, impairing its mechanosensing ability (Fig 1C). As it included eight rod subdomains (R_1-R_8), this was the longest variant studied. The third variant (mini ΔAB-Ta) lacked the Actin binding subdomain and was the shortest with only three rod subdomains (R_1-R_2-R_3), Fig 1D. Thus, our biomimetic model, which mimicked the membrane recruitment of Talin and the mechanical stretching by the Actin-Myosin, was ideally suited for investigating the molecular mechanism of Talin mechanosensing.

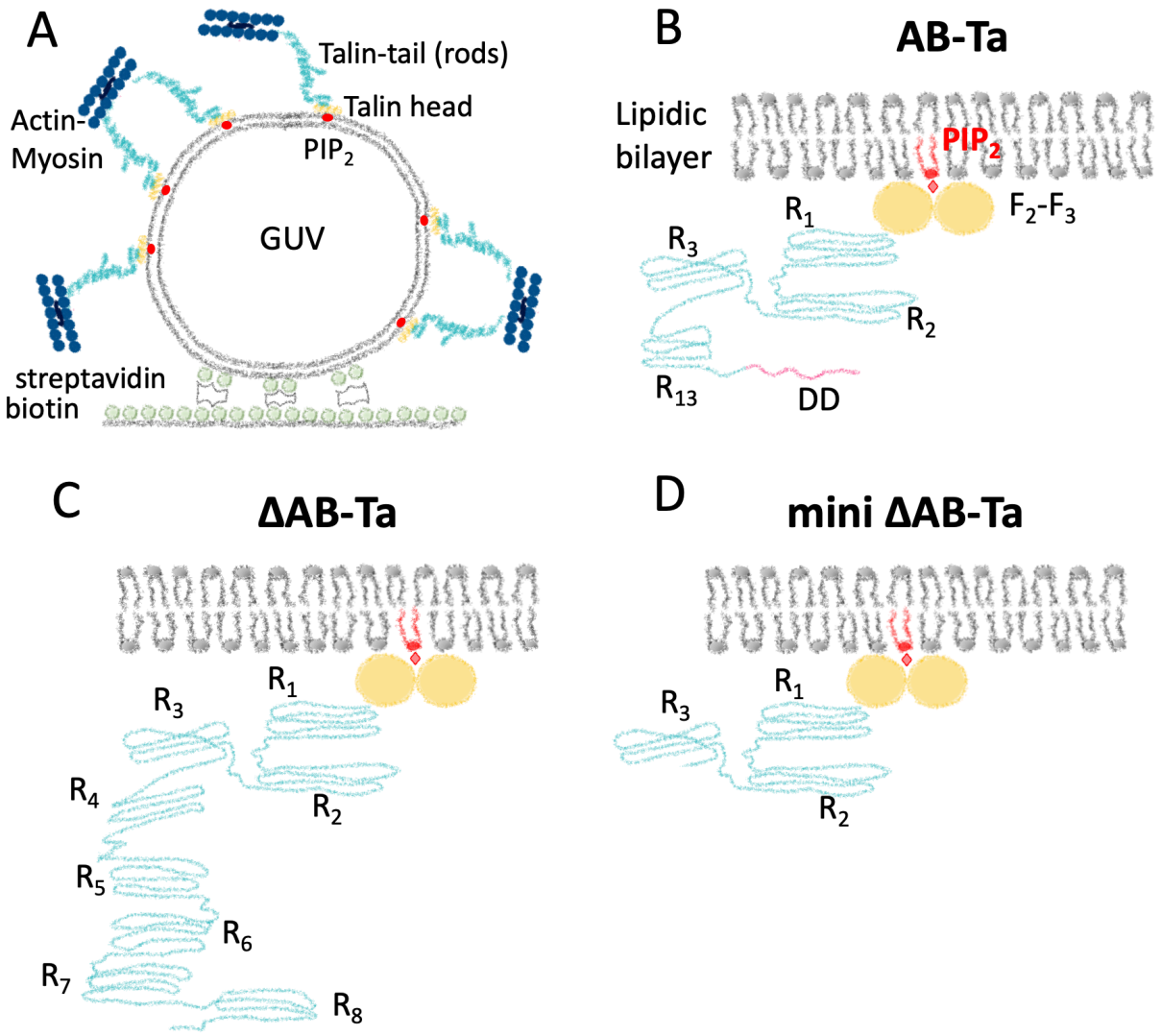

Figure 1. Talin variants associate with the membrane via PIP_2. A) Talin binds to GUVs containing PIP_2 (red) through the head domain (yellow). In a full length Talin, tail contains 13 stretchable rod subdomains (turquoise). Filamentous Actin (dark blue) binds to end of Talin tail and Talin stretching can be induced by Myosin (black) contraction. GUVs are immobilized on a biotin-streptavidin functionalized surface via biotinylated lipids B) Talin AB-Ta variant comprises four rod subdomains, one of which (R_{13}) binds to Actin, and a dimerization domain DD C) ΔAB-Ta variant comprises eight rod subdomains but no R_{13} D) mini ΔAB-Ta variant comprises three rod subdomains and no Actin binding subdomain R_{13}. All variants bind PIP_2 through a part of head domain (F_2-F_3).

QD-based FRET nanosensors act as nanomolecular ruler. To quantify the inter- and intramolecular distances of Talin variants interacting with the GUV membrane, we developed QD based FRET nanosensors. Talin variants were functionalized using QDs which bound to terminal hexahistidine (His_6) motif at Talin's tail end. MemBright640 acceptor was inserted into the GUV membrane. The coupling of orange-emitting QD with red-absorbing organic fluorophore, MemBright640, resulted in a high spectral overlap *J* (Fig S1A) and efficient FRET sensing. Narrow QDs emissions, with no red-shifted tail, allowed to collect photoluminescence intensity avoiding a bleed-through leakage to the "acceptor channel" (Fig S1B). A similar FRET pair (QD605-Cy5) has previously been employed in a single QD-based DNA sensor [23]. In this study, Talin-QD variants bound to GUV membrane and donor photoluminescence intensity (I_D) was measured. Next, MemBright640 was added to the GUVs to measure quenched photoluminescence intensity of the donor in the presence of acceptor (I_{DA}). Thus, FRET efficiencies η were calculated using equation:

$$\eta = 1 - \frac{I_{DA}}{I_D} \qquad \text{Eq. 1}$$

Since there was no spectral bleed-through between the donor and acceptor emissions, no specific correction of the I_{DA} was required. Therefore, knowing both η and the Förster distance R_0 allowed super-resolution of intermolecular interactions by measuring distances r in molecular assemblies as follows:

$$r = \left(\left(\frac{1}{\eta} - 1\right) * R_0^6\right)^{1/6} \qquad \text{Eq. 2}$$

With R_0 calculated as follows:

$$R_0 = \left(\frac{9(ln10)k^2\Phi_D J}{128\pi^5 n^4 N_A}\right)^{1/6} \qquad \text{Eq. 3}$$

where κ^2 is the orientation factor, Φ_D is the quantum yield of the donor, *J* is the overlap integral between donor emission and acceptor absorption, n is the refractive index of the medium and N_A is the Avogadro number. A critical parameter for obtaining R_0 is κ^2. Since κ^2 depends on the

transition dipole moments of the donor emission and acceptor absorption, an imprecise knowledge of the orientation of the dipole moments can lead to a significant uncertainty in the distance calculation [32]. However, QDs provide a stable and durable orientation factor due to their isotropic emission. Here, the measured emission anisotropies for Talin-QD associated to the GUV membrane and for MemBright640 were 0 and 0.02, respectively. This confirmed the value of $\kappa^2 = 2/3$ for a spherical QDs [33]. Consequently, calculated R_0 was 6.6 nm for the used orange QD-MemBright640 FRET pair. This allowed to sensitively deduce donor-acceptor distances from the plot of η over r (Fig S2A) in a distance range between circa 4 nm and 11 nm (strongest change of η with r). To achieve optimal acceptor insertion into the GUV membrane, we evaluated the integration of MemBright640 using fluorescence spectroscopy (Fig S2B). MemBright640 affinity towards the GUV was high, with an apparent dissociation constant (Kd) of 275 nM, and the GUV membrane reached saturation around 800 nM. Therefore, MemBright640 was used at 400 nM to obtain a stable intensity signal. The number of acceptors per single donor (A) must also be considered for distance calculation [34] :

$$\eta = \frac{A*R_0^6}{A*R_0^6+r^6} \qquad \text{Eq. 4}$$

Based on a theoretical prediction of the mini ΔAB-Ta structure (see AlphaFold in Supporting Information), we assumed that r = 6.4 nm. The η found at 400 nM MemBright640 was 0.58 (Fig S2C) which resulted in A~1. Thus, our experiments were designed to easily quantify molecular distances using a 1:1 donor-acceptor ratio.

Intermolecular interaction measured between Talin variants and GUV membrane is in the 6-9 nanometer range. First, intermolecular distances were measured using fluorescence spectroscopy. Talin variants were conjugated with QD donors and then mixed with GUVs to allow membrane-protein assembly. To prevent an excess of unbound QDs, QD was conjugated with Talin variants at a ratio of 1:2 (Fig S3). QDs were excited at 405 nm, and the

resulting photoluminescence spectra (Fig 2A,B,C, orange curves) showed their maximum intensity at ~600 nm. The interaction between Talin and the GUV membrane was demonstrated upon the addition of MemBright640 acceptor, as illustrated by the quenched photoluminescence intensity (Fig 2 A,B,C, blue curves). In addition to donor quenching, the acceptor showed weak sensitization at ~650 nm. Using the integrated areas of the donor and donor-acceptor spectra to calculate I_D and I_{DA}, respectively, η was determined using Eq. 1. Corresponding η values of 0.48, 0.36, and 0.53, were found for the three Talin variants, mini ΔAB-Ta, ΔAB-Ta and AB-Ta, respectively (Fig 2D, Table 1). Eq. 2 was used to determine the distance between QD donor and MemBright640 acceptor. For mini ΔAB-Ta, ΔAB-Ta and AB-Ta, the calculated distances were 6.7, 7.3 and 6.5 nm, respectively (Table 1). Since QD was at the tail end of Talin, these distances reflected intermolecular distances separating Talin from the GUV membrane. However, spectroscopic experiments were performed at the population level. We were therefore interested in performing experiments that could represent cell biology research at the single cell level. Since imaging allows to perform measurements of individual GUVs, we reproduced our experiments using fluorescence microscopy.

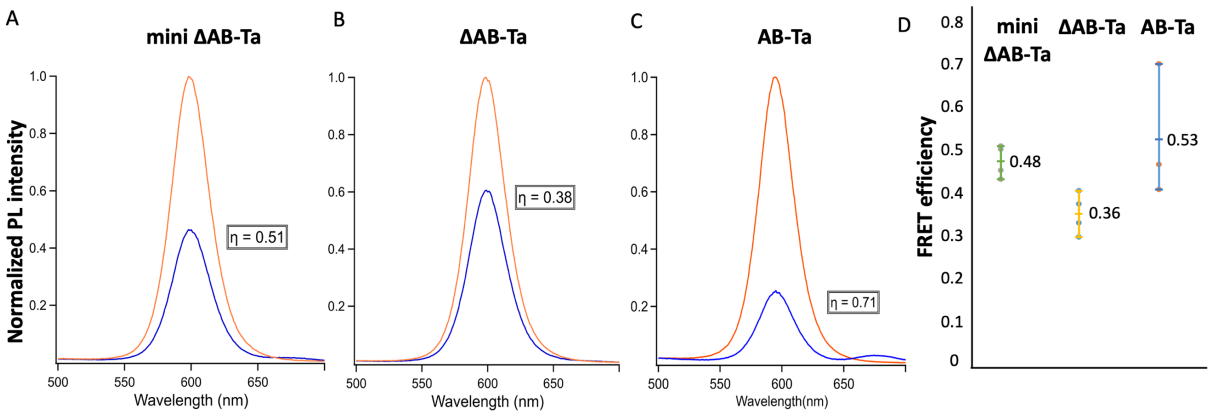

Figure 2. Talin-GUV membrane interaction quantified using fluorescence spectroscopy. Normalized photoluminescence spectra of A) mini ΔAB-Ta, B) ΔAB-Ta and C) AB-Ta QD conjugated (donor) are shown by the orange curves. Normalized photoluminescence spectra of those Talin-QD variants quenched by MemBright640 acceptor are shown by the blue curves. Corresponding η are shown in black boxes. λex= 405 nm. D) Diagram of corresponding η for three Talin variants. The results shown were confirmed in N=4 (mini ΔAB-Ta and ΔAB-Ta) or N=3 (AB-Ta) independent experiments.

Table 1. Comparison of FRET efficiencies η and distances r obtained using spectroscopy and microscopy for mini ΔAB-Ta, ΔAB-Ta, AB-Ta and AB-Ta stretched by Actin-Myosin. Sub-population 1 and 2 are sub-populations of values found using microscopy. δ are standard deviations.

	Spectroscopy				Microscopy			
	η	δ_η	r (nm)	δ_r	η	δ_η	r (nm)	δ_r
mini ΔAB-Ta	0.48	0.04	6.7	0.2	0.38	0.13	7.3	0.8
ΔAB-Ta	0.36	0.05	7.3	0.2	0.17	0.08	8.8	0.9
AB-Ta	0.53	0.16	6.5	0.7	0.44	0.19	6.9	0.9
AB-Ta sub-population 1	x	x	x	x	0.34	0.08	7.4	0.5
AB-Ta sub-population 2	x	x	x	x	0.71	0.07	5.7	0.4
AB-Ta + Actin-Myosin	0.63	0.04	6	0.1	0.74	0.17	5.5	0.8
AB-Ta + Actin-Myosin sub-population 1	x	x	x	x	0.54	0.13	6.4	0.6
AB-Ta + Actin-Myosin sub-population 2	x	x	x	x	0.85	0.03	4.9	0.2

Similarly to spectroscopy, GUVs were incubated with Talin-QD variants. To enable identification of the same GUV in two-step imaging (acquisition of I_D and I_{DA}), GUVs were immobilized on biotin-streptavidin functionalized surfaces using biotinylated lipids incorporated in the GUV membrane (Fig 1A). First, images were captured in the "donor channel", where QD donors were excited at λ=405 nm and their intensities collected at λ=607 nm. Mean I_D values were extracted from the membrane region for each GUV (Fig 3 A_1 ,B_1 ,C_1). After the addition of MemBright640, images were captured in the same channel to obtain I_{DA} (Fig 3 A_2, B_2 ,C_2). The most pronounced difference in intensity, between I_D and I_{DA} images, corresponded to a high η (e.g., AB-Ta on Fig 3C_1 and C_2) which means that the shortening of the intermolecular distance made the quenching of the donor more visible. Prior to the addition of MemBright640, the sample served as non-biosensing control (Fig 3A_3 ,B_3 ,C_3). To compare with conventional FRET imaging, images were also acquired in the "biosensing channel". QD donors were excited at λ=405 nm, and emission from the MemBright640 acceptor was collected at λ=692 nm (Fig 3A_4,B_4 ,C_4). Differences in intensity were also observed, but were not quantified due to a relatively weak fluorescence signal, as already found in the spectroscopy experiments (Fig 2). Thus, η for each individual GUV, represented by data points in the violin

plot (Fig 3D) was calculated using Eq 1. For mini ΔAB-Ta and ΔAB-Ta, η was 0.38 and 0.17, respectively (Table 1), and the violin plots showed a single population of values. In contrast, for AB-Ta, we found two sets of values: η_1=0.34 and η_2=0.71 (Fig 3D, Table 1). Since Talin contains a dimerization domain, those two sets suggested that monomers and dimers of AB-Ta are not located at the same distance from the membrane. Further, the C-terminal 32 amino acids long His_6-tag, for QD binding, might contribute to the spread of data points within populations, as shown by the violin plot. For ΔAB-Ta and mini ΔAB-Ta, their His_6-tags were much shorter (8 amino acids). Kruskal-Wallis test followed by Conover paired comparisons confirmed the significant differences between ΔAB-Ta and AB-Ta or mini ΔAB-Ta (Fig 3D). To solve the orientation of Talin with respect to the membrane, structural predictions were generated using AlphaFold machine learning approach [35]. However, the predicted structures were not relevant because those were mostly based on the autoinhibited Talin structure and did not account for the Talin-membrane interaction (see Supporting Information and Fig S4 and S5). In summary, the imaging experiments provided intermolecular distances of 7.4 ± 0.5 and 5.7 ± 0.4 nm for two sub-populations of AB-Ta variant, as well as 7.3 ± 0.8 nm and 8.8 ± 0.9, for mini ΔAB-Ta and ΔAB-Ta variants, respectively (Table 1). As for the spectroscopy experiments, the distance increased from mini ΔAB-Ta to ΔAB-Ta. Imaging on a single GUV revealed information hidden within an entire population obtained via spectroscopy. η obtained by spectroscopy were higher than those obtained using microscopy. This could be explained by differences in experimental conditions. We assume that some of the ensemble GUVs exploded after the acceptor addition and settled in the cuvette, resulting in an I_{DA} decrease and thus, a biased η.

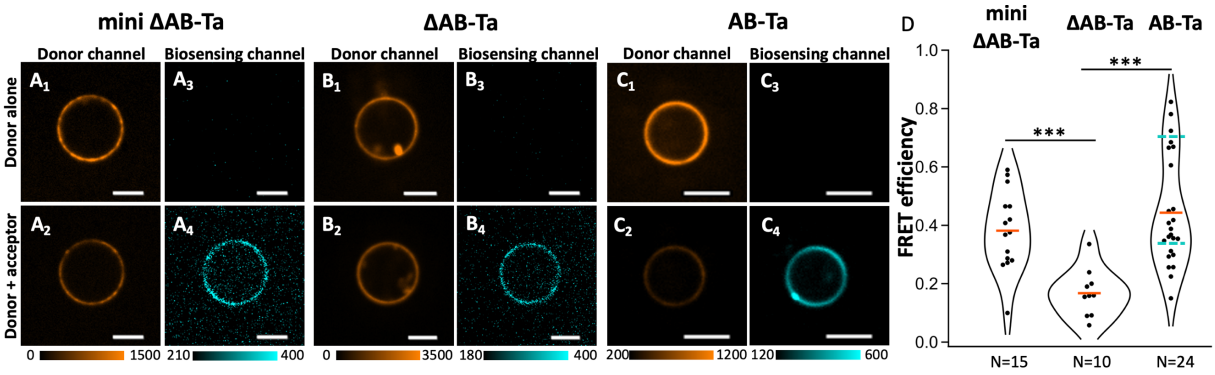

Figure 3. Talin-membrane interaction quantified using single-GUV fluorescence microscopy. Representative fluorescence images of three Talin variants: A) mini ΔAB-Ta, B) ΔAB-Ta, and C) AB-Ta. In the "donor channel" photoluminescence intensity of the QD donor before (A_1, B_1, C_1) and after addition of the acceptor (A_2, B_2, C_2). In the "biosensing channel", there was no interaction detected when the donor was alone (A_3, B_3, C_3). Alternatively, acceptor emission occurred due to the sensitization by the donor (A_4, B_4, C_4). "Donor channel": λex= 405 nm, λem= 607/36 nm, "biosensing channel": λex= 405 nm, λem= 692/40 nm, color bars below images represent intensity level, scale bars = 5 μm. D) Violin plot of η for three Talin variants. Each spot represents a single GUV and orange bars present mean values with η=0.38 for mini ΔAB-Ta, η=0.17 for ΔAB-Ta, and η=0.44 for AB-Ta. Turquoise bars represent mean values of sub-populations with η_1=0.34 and η_2=0.71. The number of analyzed GUVs is indicated below the plots and the results presented were confirmed in N=3-4 independent experiments. Significantly different data (p<0.01) are indicated by 3 stars.

Mechanosensing causes Talin to organize parallel to the membrane. Actin and Myosin II, two major filament components, have been used to mimic the tensile force of the cytoskeleton. To measure the intramolecular changes in Talin length, we used the AB-Ta variant. AB-Ta-QD was assembled with the GUV membranes. AB-Ta variant contained Actin binding subdomain R_{13}. Upon addition of Myosin, the Actin filaments contracted inducing AB-Ta stretching. Corresponding I_D was measured using both spectroscopy and microscopy (Fig S6A,B_1). The FRET nanosensor was completed with MemBright640 acceptor and the quenching of the QD donor I_{DA} was recorded (Fig 4A, S6A,B_2). To demonstrate the nanosensor insertion, images were recorded in both the "acceptor" and "biosensing channels" (Fig 4B,C). In the "Actin channel", Actin bound to Talin and polymerized along the GUV (white arrows, Fig 4D_2,D_3) which could be distinguished from a layer of filaments forming a network around the GUV. 3D images were reconstructed from z-stacks, and their top and lateral views are

shown in Figures 4A_2,B_2,C_2,D_2 and 4A_3,B_3,C_3,D_3 respectively. Spectroscopy as well as microscopy experiments revealed a slight increase in a mean η value (Fig 4E,F) between unstretched (left) and stretched (right) AB-Ta. As above, spectroscopy showed a net difference in distances, while microscopy revealed two distinct sub-populations. Thanks to spectroscopy, we were able to measure a η displacement from 0.53 to 0.63, which corresponds to AB-Ta tail end approaching the membrane from 6.5 to 6 nm (Table 1). Measurements using microscopy were more precise with values of η_1 =0.34 and η_2 =0.71 for unstretched and η_1 =0.54 and η_2 =0.85 for stretched AB-Ta. This suggested that when Talin is unstretched, some tail ends are located at 7.4 ± 0.5 and others at 5.7 ± 0.4 nm (Table 1). In contrast, when Actin-Myosin exerted tension on AB-Ta variant, tail ends relocated at 6.4 ± 0.6 nm and 4.9 ± 0.2 nm. Mean η values (Fig 4F), as well η_1 and η_2 of sub-populations comparing stretched and unstretched conditions were significantly different. According to Gaussian distribution for QD:AB-Ta conjugated at ratio 1:2 , the majority of AB-Ta variants were dimers, some remained monomers. This suggests that AB-Ta dimers undergo Actin-Myosin stretching, corresponding to a decrease in the distance between the tail end of Talin and the membrane of 2.5 nm, from 7.4 (bottom left of the violin plot in Fig. 4E) to 4.9 nm (top right of the same plot). This decreased distance indicates a significant elongation of the Talin parallel to the membrane. In this scenario, Actin attach to R_{13} and Myosin contracts the polymerized Actin filaments along the membrane (Fig 5B), visible in Figure 4D_2 and D_3 (white arrows). The less widespread distance sub-population may correspond to AB-Ta monomers, i.e., 5.7 (top left of the violin plot in Fig. 4E) extended to 6.4 nm (bottom right of the same plot) but not parallel to the GUV membrane.

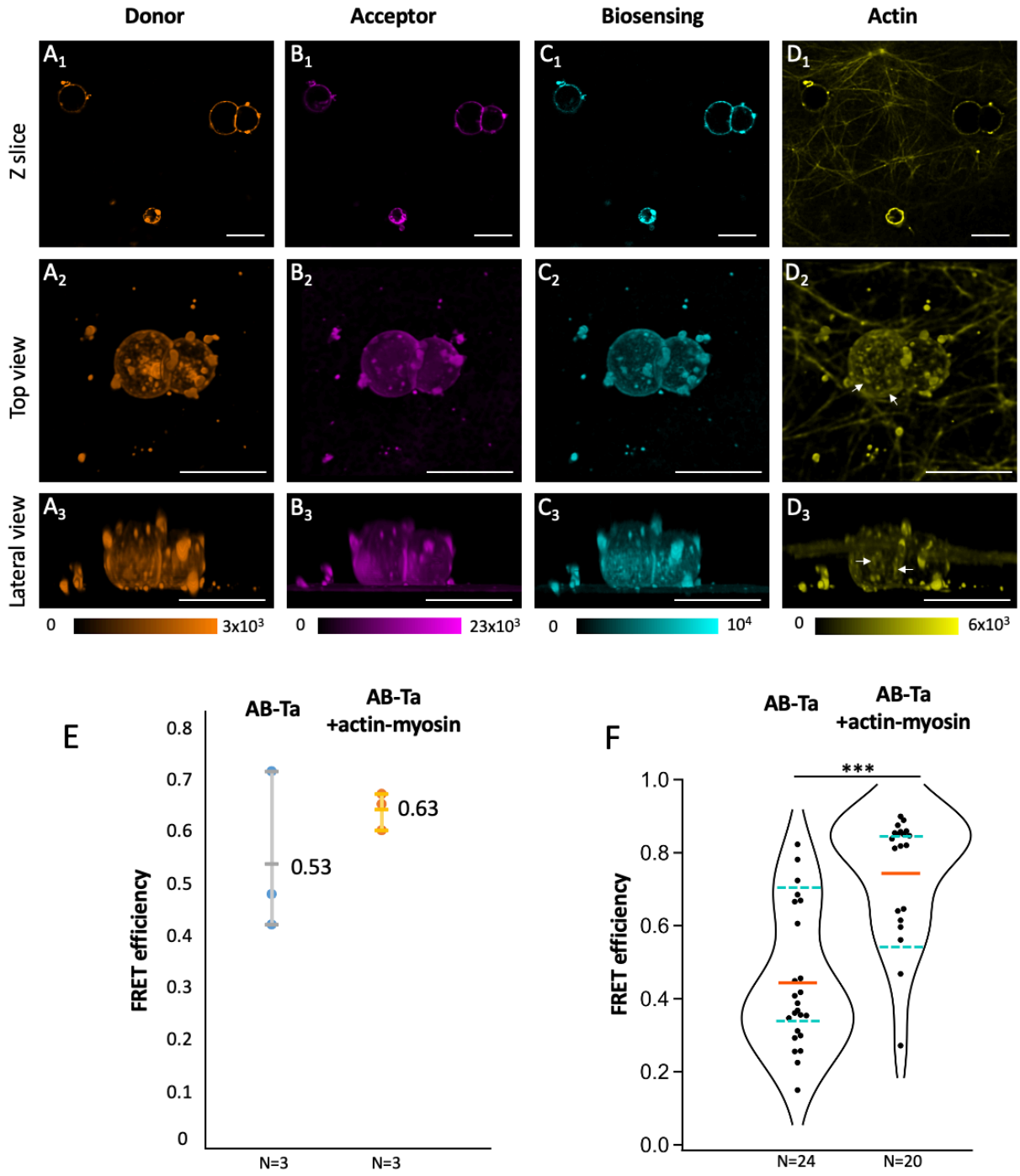

Figure 4. Quantification of Talin mechanosensing. A-D) Fluorescence microscopy of FRET nanosensor of AB-Ta variant stretched by Actin-Myosin in A) the "donor channel" (photoluminescence intensity of the QD, λex= 405 nm, λem= 607/36 nm), B) the "acceptor channel" (fluorescence of MemBright640, λex= 642 nm, λem= 692/40 nm), C) the "biosensing channel" (donor excited and sensitized acceptor emitting, λex= 405 nm, λem= 692/40 nm) and D) the "Actin channel" (fluorescence of Actin labeled by Atto488, λex= 488 nm, λem= 525/45 nm). White arrows indicate Actin-Myosin fibers on the GUVs. A_1-D_1) Z-slice from a stack with few GUVs in the imaged area. A_2-D_2) Top view of the deconvolved 3D image of upper right GUVs on A_1-D_1. A_3-D_3) Lateral view of the deconvolved 3D image of the same GUVs. Color

bars represent intensity level, scale bars = 10 μm. E) Diagram of η calculated from spectroscopy experiments for AB-Ta +/- Actin-Myosin. The results presented were confirmed in N=3 independent experiments. F) Violin plot of η for AB-Ta +/- Actin-Myosin. Each spot represents a single GUVs, orange bars present η mean values with η=0.44 (left, unstretched AB-Ta variant) and η=0.74 (right, stretched AB-Ta variant). Turquoise bars represent η mean values of sub-populations with η_1=0.34 and η_2=0.71 (left, unstretched AB-Ta variant) and η_1=0.54 and η_2=0.85 (right, stretched AB-Ta variant). The number of analyzed GUVs is indicated below the plots and the results presented were confirmed in N=2-3 independent experiments. Significantly different data ($p<0.001$) are indicated by 3 stars.

CONCLUSIONS

In conclusion, we have demonstrated that QD-based FRET nanosensors can be used to quantify the assembly of FA proteins on a synthetic membrane. The distances between proteins and the membrane surface could be measured with an accuracy of less than 1 nm. Distances obtained through microscopy were more effective than spectroscopy in identifying differences within the same population. The microscopy results suggest that AB-Ta dimers undergo Actin-Myosin stretching, corresponding to a decrease in the distance between the distal edge of Talin and the membrane of 2.5 nm (from 7.4 to 4.9 nm).

We showed that a minimal set of proteins, including Talin, Actin and Myosin is able to initiate a mechanosensing process even in absence of Talin binding partners such as Vinculin. Vinculin is necessary to build a 3D scaffold and regulate the mechanical response of the adhesion. Two different mechanisms for linking Talin with the Actin-Myosin machinery were proposed [36][37]. The first one stipulates that Actin binds to R_{13}, then Actin-Myosin contract and stretch R_2-R_3 at the opposite, allowing Vinculin binding. The second mechanism proposes the release of inhibition of R_2-R_3 by the Vinculin direct binding. This would allow Actin to bind to Talin independently of R_{13} (on other Actin binding sites). Therefore, our results support findings that mechanosensing is likely initiated by the Actin-Myosin stretching initiating at R_{13}

subdomain, as determined via AFM and magnetic tweezers [14], [38]. This initial mechanosensing step causes Talin to become linearized and move closer to the membrane (Fig 5). Super-resolution microscopy was used to obtain information on the molecular conformation and geometry of Talin in mature adhesions, where it is tilted at a 15° angle from the membrane. This revealed that Talin determines the nanoscale architecture of the FA, acting as a molecular ruler [4]. Therefore, we propose that in nascent adhesions, Talin is first immobilized in PIP_2-enriched nanodomains (Fig 5A). Due to the nanometric diameter of the PIP_2 clusters of approximately 10 to 50 nm, they could not be resolved under our diffraction-limited imaging conditions [39]. Talin is then captured by Actin filaments that polymerize at the R_{13} subdomain. These Actin filaments are stretched by Myosin in the vicinity of the membrane, at ~5 nm (Fig 5B). Eventually, the binding of Vinculin results in the tilting of Talin. In conclusion, QD-based FRET nanosensors have yielded quantitative insights into Talin stretching dynamics. Using these tools, we will be able to elucidate emerging models for Talin assembly with various partners.

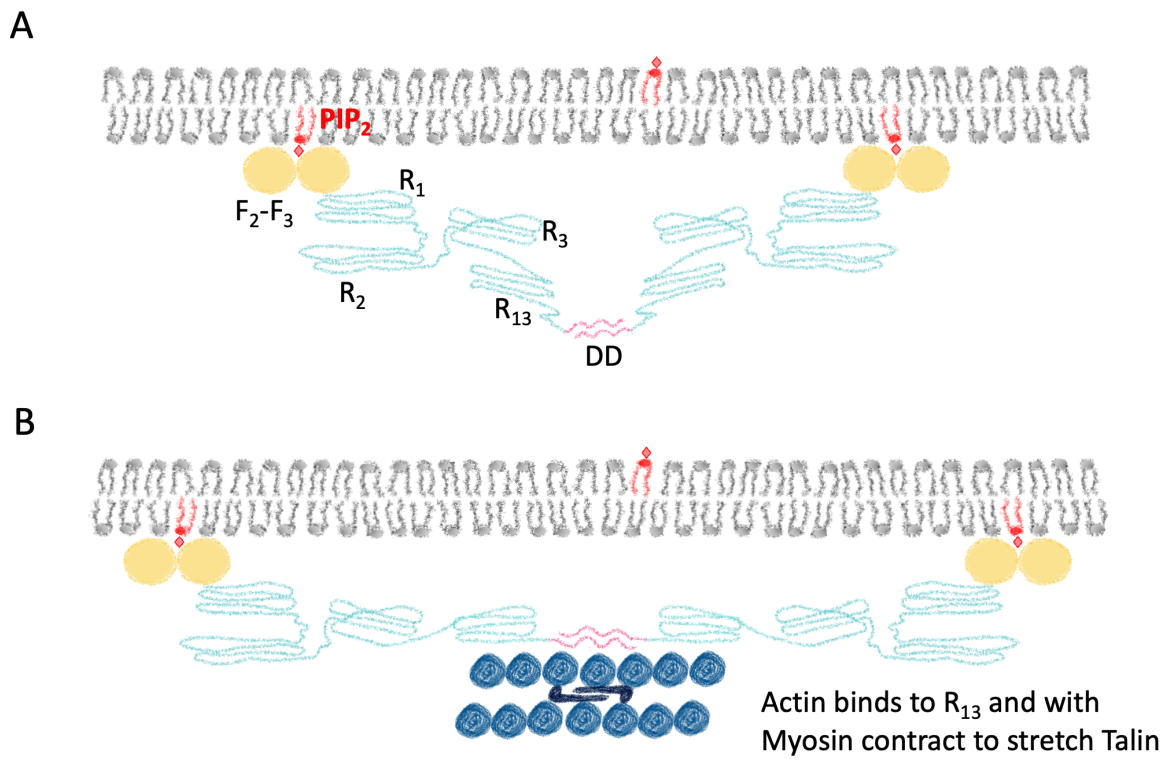

Figure 5. Model of early Talin mechanosensing in nascent adhesions in the example of AB-Ta. A) Talin dimerizes through its dimerization domain DD. The interaction with PIP_2 immobilizes Talin and releases its autoinhibition. B) Actin binds to R_{13}, polymerizes, and Actin-Myosin stretches Talin parallel to the membrane to expose R_2-R_3 for Vinculin binding.

EXPERIMENTAL SECTION

FRET nanosensors. CdSe/CdS/CdZnS/ZnS core/multishell QDs were prepared and coated with CL4 capping ligands as described previously [40]. The FRET nanoprobes were prepared by mixing orange QD (λ_{em}=600 nm) at 20 nM and Talin variants in a 1:2 concentration ratio in KCl 100 mM,HEPES 20 mM pH 7.4 or KCl 100 mM, Tris 20 mM pH 7.8 buffers supplemented with 0.06% BSA for 1h on ice. QD bound to Talin's tail end though a coordination bond with hexa-histidine (His_6) linker. Talin-QD conjugate was added on GUVs. Later, MemBright640 acceptor (λ_{em}=664 nm) was diluted at 200/400 nM in the same buffer and added for integration in GUV lipidic bilayer for 30 min at room temperature. This probe formed micelles in aqueous buffers, which ultimately causes fluorescence quenching [41]. The fluorescence was restored when the probe permeated the outer side of the lipid bilayer.

Recombinant Talin variants. Three Talin-1 variants recombinant proteins were produced in *E.coli* bacteria strain (BL21 DE3, Invitrogen). AB-Ta (Actin binding Talin) variant, composed of F_2-F_3-R_1-R_2-R_3-R_{13}, was cloned into pETM plasmid and expressed as fusion protein with a StrepTagII at the N-terminus and His_6-tag at the C-terminus [42]. ΔAB-Ta (delta Actin-binding Talin) and mini ΔAB-Ta (mini delta Actin-binding Talin) were cloned into pGEX6P1 plasmid (GE Healthcare) and expressed as fusion proteins with GST-tag at the N-terminus and His_6-tag at the C-terminus [42]. Talin variants were purified by two-step affinity chromatography through the StrepTag using Strep-Tactin Sepharose (Cytiva) or the GST-tag using Glutathione

Sepharose and PreScission protease (GE Healthcare) and His_6-tag using (Ni2+-nitrilotriaceticacid)-Agarose (Macherey-Nalgene).

Actin. Actin was purified from rabbit skeletal muscle acetone powder and after gel filtration kept at 4°C in G buffer (5 mM Tris-HCl, pH 7.8, 0.2 mM ATP, 0.1 mM $CaCl_2$, 0.1 mM DTT, 0.01% NaN_3) [43]. Actin was labeled on lysins with NHS-ester Atto-488 using standard procedures.

Myosin. Myosin II was purified from rabbit muscle following the method described by Pollard [44].

GUV preparation. GUVs were prepared by using the polyvinyl alcohol (PVA) gel-assisted vesicle formation based on Weinberger et al. method [45]. Briefly, PVA was dissolved at 5 % (w/w) in a 280 mM sucrose solution containing 20 mM Tris-HCl pH 7.5. The PVA solution, heated to 50°C, was spread onto 22×22 mm glass coverslips, previously cleaned by sonication in Milli-Q water (Merck), ethanol and Milli-Q water sequentially (10 min each). The PVA-coated coverslips were incubated at 37°C ON. Lipids were mixed in chloroform at a concentration of 1 mg/ml. The lipid mixtures we used contain L-α-phosphatidylcholine (egg PC) with 20 % mole cholesterol, 10 % mole brain L-α- phosphatidylinositol-4,5-bisphosphate (PIP_2) and 3.5 % mole 1,2-distearoyl-sn-glycero-3-phosphoethanolamine N[biotinyl(polyethylene glycol)-2000] (ammonium salt) (DSPE-(PEG2000)-biotin). 10 µl of the lipid mixture was spread on PVA-coated coverslips using a Hamilton syringe and vacuum-dried for 30 min at RT. Around 1 ml of 200 mM sucrose solution was added on the top of every coverslip. GUVs were formed by incubation for 2.5 h at 18°C. Eventually, the GUVs were collected, centrifuged at 14,000 g for 30 min, and stored in glass vials at 4°C for 2-3 days.

Surface functionalization. GUVs were immobilized on the glass surfaces using electrostatic attraction (on PLL-PEG) or specific biomolecular interaction (biotin-streptavidin). The most of experiences were performed on biotin streptavidin coated surfaces. 22 mm diameter coverslips (Paul Marienfeld GmbH & Co. KG, ref.0111620) were cleaned by sonication in Milli-Q water (Merck), ethanol 96 % and Milli-Q water sequentially (10 min each). Coverslips were exposed for one minute to UV ozone cleaner (Ossila E511) to deprotonate the surface. Then, coverslips were incubated for 1h in Biotin-PEG-Silane (Laysan Bio, MW 3400) at 10 mg/mL in DMSO. Surfaces were washed with Milli-Q water and dried with pressurized air. The functionalized surfaces were either used for further functionalization or stored at 4°C for the following day. Next, coverslips were incubated with streptavidin (iba, Cat.No. 2-0203-100) at 1 mg/mL in 20 mM HEPES for 30 min, washed with Milli-Q water and dried with pressurized air. For strep-tagged AB-Ta variant, we sustained biotin-streptavidin functionalization to PLL-PEG to avoid unspecific binding of Talin to streptavidin on coated surface. Coverslips were cleaned as previously and then incubated for 1 h with 0.1 mg/mL PLL-g-PEG (SuSoS, LT01-11) in 20 mM HEPES pH 7.4 and washed with milliQ water and dried with pressurized air. Finally, coverslips were placed in the incubation chamber (Chamlide CMB for 22mm round coverslips) for further observation.

Sample preparation. The sample was prepared as partially mentioned in the FRET nanosensors part, by mixing QD and Talin into the buffer (KCL 100 mM, HEPES 20 mM pH 7.4 for FRET biosensing experiments or KCl 100 mM, Tris 20 mM pH 7.8 for mechanosensing detection) and BSA in a total volume of 300 μL. The mixture was incubated for 1 h on ice. Later on, 300 μL of 50 % of GUVs and 50 % of 200 mM sucrose solution was added to the mixture and incubated for 30 min on ice. The preparation was then deposited in the observation chamber and incubated for 1 h at room temperature to leave GUVs bind to the surface. For mechanosensing experiments, a mixture of 2 μM Actin (non fluorescent or 10 % Atto488

labeled) and 50 nM Myosin was prepared in Actin polymerization buffer (100 mM KCl, 0.2mM ATP, 1 mM $MgCl_2$, 0.2 mM EGTA, 20 mM DTT with ATP regeneration mix consisting of 10 mM creatine phosphate, (3.5U/mL) creatine kinase, 2 mM ATP, 2 mM $MgCl_2$). The Actin-Myosin mixture was added to the sample in the chamber and incubated for 30 min.

Spectroscopy. Spectroscopy experiments were conducted on FluoroMax-4 spectrofluorometer (Horiba Scientific). Emission spectra of donor alone and donor in the presence of the acceptor were acquired using 625 V gain, 2 nm slit range, and excitation 405 nm.

Microscopy. All FRET nanosensor optimization experiments were conducted on a conventional wide-field EPI-fluorescence microscope (Olympus IX71) and illuminated with an X-Cite 120Q mercury source (EXFO Photonic Solutions Inc.) at ~90 mW/cm^2. Emission of QD donor was acquired using a 60x objective (UPLSAPO, Olympus), and with 365 nm excitation filter (Hg01–365-25); 495 nm dichroic mirror (FF495-Di03) and a 600 nm emission filter (FF01- 605/15-25). All filters were purchased from Semrock. Images were recorded using a sCMOS camera (pco.edge, PCO) with an acquisition time of 300 ms. In order to provide biosensing images (Fig 3 A_3,A_4,B_3,B_4,C_3,C_4 and 5 B_3,B_4) we used spinning-disc microscope (Yokogawa CSU-X1-A1) at Light Microscopy Facility (I2BC) on a Nikon Ti Eclipse E microscope equipped with a 60X oil immersion objective (Apochromat, 1.49 NA) and coupled to a sCMOS camera (Photometrics, Prime 95B). In "biosensing channel" QD donors were excited with 405 nm laser and MemBright640 emission collected though quad dichroic and 692/40 nm emission band pass filter. In "donor channel" QDs were excited with 405 nm laser and donor emission collected though quad dichroic and 607/36 nm emission band pass filter. In "acceptor channel" MemBright640 was excited with 642 nm laser and its emission collected though quad dichroic and 692/40 nm emission band pass filter. Images were acquired at 10 % laser power using Metamorph software. 3D images were performed with 0.3 μm steps in "donor channel", "biosensing channel", "acceptor channel". For this experiment images were also

taken in “Actin channel”. Actin-Atto488 (at 10 %) was excited with 488 nm laser and its emission collected though quad dichroic and 525/45 nm emission band pass filter.

Data analysis. Emission spectra registered using spectroscopy were analyzed using Igor Pro 9 (WaveMetrics). The signal under the curve was integrated for donor alone and donor in the presence of acceptor. Corresponding FRET efficiencies were calculated using Eq.1. Images of GUVs in donor alone and donor in the presence of acceptor were analyzed with Icy software (Institut Pasteur). Using “Thresholder” plugin we determined single ROI for each GUV where upper threshold value is the max intensity and the lower one, the background of the image. Corresponding FRET efficiencies were calculated using Eq.1. AlphaFold predictions were generated using AlphaFold@I2BC platform. AlphaFold is a new machine learning approach that uses protein structural data, based on multi-sequence alignments, to design the deep learning algorithm[35]. 3D GUV images (Fig 4) were deconvolved using Huygens Essential software. Taking into account the camera and image acquisition characteristics, parameters were adjusted with an image sampling of 153 nm in X and Y-axis and 300 nm in Z-axis. A relative Nyquist rate of 0.268 in X and Y-axis and 0.328 for Z-axis was also deduced. The original image was deconvolved with Classic MLE (Maximum Likelihood Estimation) as the deconvolution algorithm and a standard strategy for initial values. An approximative number of 30 iterations and quality threshold of 0.01 was used in the setup.

Statistics. The FRET efficiencies of AB-Ta, ΔAB-Ta, and mini ΔAB-Ta (Fig 3) were compared by a non-parametric Kruskal-Wallis test followed by Conover paired comparisons. The FRET efficiencies of AB-Ta and AB-Ta + Actin-Myosin were compared by a non-parametric Mann-Whitney (Fig 4). The numbers of GUVs used and of independent replicates are specified in corresponding Figures. All statistical tests were performed using the online software BrighStats (https://secure.brightstat.com/index.php).

Agarose gel electrophoresis. Gel electrophoresis was performed on QDs, and QDs conjugated with Talin variants to demonstrate self-assembly at ratios 1:1 (QD to protein) and 1:2. QDs at 1 μM were self-assembled with 1 μM (1:1 ratio) or 2 μM (1:2 ratio) AB-Ta, ΔAB-Ta and mini ΔAB-Ta for 1h in Tris-borate-EDTA (TBE) 0.5x. Bromophenol Blue (Mass Ruler, Thermo Scientific, R0621) was added at a ratio of 1:6 to a total volume of 15 μL. Agarose gel was prepared by melting agarose (UltraPure, Invitrogen, 16500-500) in TBE 0.5x in a microwave oven until the solution boiled. The agarose was cooled under fresh running water (to reach T~60°) and poured and allowed to polymerize at room temperature for 20 min and hydrated in TBE 0.5x for an additional 20 min. All samples were run for 15 min in TBE 0.5x buffer at 80 V. Samples were imaged under UV exciter plate (ChemiDoc Imaging system, BioRad).

Fluorescence anisotropy. k^2 value was measured using fluorescence anisotropy (Xenius, Safas monaco spectrofluorometer). Thus, in GUVs carrying Talin-QD and MemBright 640 registered emission anisotropies were 0 for QDs and 0.02 for MemBright640. In consequence, in our experiments the most probable k^2 worth and was calculated following equation:

$k^2 = (2 - a - d + 3ad)/3$

where a and d are respectively acceptor and donor emission anisotropies [46].

Author Contributions

The manuscript was written through contributions of all authors. All authors have given approval to the final version of the manuscript.

Conflict of Interest

The authors declare no conflict of interest.

ACKNOWLEDGMENT

This work was partially funded by the Interdisciplinary Object “OI Bioprobe” from Université Paris Saclay. Authors thank the Light Microscopy facility of Imagerie-Gif for access to spinning disc microscope and Integrative Bioinformatics platform (BIOI2) for free use of AlphaFold@I2BC. Authors thank also Bruno Faivre and Clémence Vigouroux for purification of Talin variants.

ABBREVIATIONS

Talin variants:

AB-Ta, Actin binding Talin (composed of F_2-F_3-R_1-R_2-R_3-R_{13}); ΔAB-Ta, delta Actin-binding Talin (composed of F_2-F_3-R_1-R_2-R_3-R_4-R_5-R_6 R_7-R_8); mini ΔAB-Ta, mini delta Actin-binding Talin (composed of F_2-F_3-R_1-R_2-R_3)

FA, focal adhesion; FP, fluorescent protein; FRET, Förster resonance energy transfer; GUV, giant unilamellar vesicle; His_6, hexa-histidine, PIP_2, phosphatidylinositol 4,5-bisphosphate; PVA, polyvinyl alcohol; QD, quantum dot;

REFERENCES

[1] P. Kanchanawong *et al.*, "Nanoscale architecture of integrin-based cell adhesions," *Nature*, vol. 468, no. 7323, pp. 580–584, Nov. 2010.

[2] K. Legerstee and A. Houtsmuller, "A Layered View on Focal Adhesions," *Biology (Basel).*, vol. 10, no. 11, p. 1189, Nov. 2021.

[3] L. B. Case and C. M. Waterman, "Integration of actin dynamics and cell adhesion by a three-dimensional, mechanosensitive molecular clutch," *Nat. Cell Biol.*, vol. 17, no. 8, pp. 955–963, Aug. 2015.

[4] J. Liu *et al.*, "Talin determines the nanoscale architecture of focal adhesions," *Proc. Natl. Acad. Sci.*, vol. 112, no. 35, pp. E4864–E4873, Sep. 2015.

[5] X. Song *et al.*, "A novel membrane-dependent on/off switch mechanism of talin FERM domain at sites of cell adhesion," *Cell Res.*, vol. 22, no. 11, pp. 1533–1545, Nov. 2012.

[6] B. T. Goult *et al.*, "The Structure of an Interdomain Complex That Regulates Talin Activity," *J. Biol. Chem.*, vol. 284, no. 22, pp. 15097–15106, May 2009.

[7] K. Chinthalapudi, E. S. Rangarajan, and T. Izard, "The interaction of talin with the cell membrane is essential for integrin activation and focal adhesion formation," *Proc. Natl. Acad. Sci.*, vol. 115, no. 41, pp. 10339–10344, Oct. 2018.

[8] J. Pernier *et al.*, "Talin and kindlin cooperate to control the density of integrin clusters," *J. Cell Sci.*, vol. 136, no. 8, Apr. 2023.

[9] D. Dedden *et al.*, "The Architecture of Talin1 Reveals an Autoinhibition Mechanism," *Cell*, vol. 179, no. 1, pp. 120-131.e13, Sep. 2019.

[10] A. Haage *et al.*, "Talin Autoinhibition Regulates Cell-ECM Adhesion Dynamics and Wound Healing In Vivo," *Cell Rep.*, vol. 25, no. 9, pp. 2401-2416.e5, Nov. 2018.

[11] O. Vinogradova *et al.*, "A Structural Mechanism of Integrin αIIbβ3 'Inside-Out' Activation as Regulated by Its Cytoplasmic Face," *Cell*, vol. 110, no. 5, pp. 587–597, Sep. 2002.

[12] L. M. Owen, N. A. Bax, W. I. Weis, and A. R. Dunn, "The C-terminal actin-binding domain of talin forms an asymmetric catch bond with F-actin," *Proc. Natl. Acad. Sci.*, vol. 119, no. 10, pp. 18–20, Mar. 2022.

[13] X. Hu *et al.*, "Cooperative Vinculin Binding to Talin Mapped by Time-Resolved Super Resolution Microscopy," *Nano Lett.*, vol. 16, no. 7, pp. 4062–4068, Jul. 2016.

[14] M. Yao *et al.*, "The mechanical response of talin," *Nat. Commun.*, vol. 7, no. 1, p. 11966, Sep. 2016.

[15] F. Margadant *et al.*, "Mechanotransduction In Vivo by Repeated Talin Stretch-Relaxation Events Depends upon Vinculin," *PLoS Biol.*, vol. 9, no. 12, p. e1001223, Dec. 2011.

[16] B. Hochreiter, M. Kunze, B. Moser, and J. A. Schmid, "Advanced FRET normalization allows quantitative analysis of protein interactions including stoichiometries and relative affinities in living cells," *Sci. Rep.*, vol. 9, no. 1, p. 8233, Dec. 2019.

[17] G. Bunt and F. S. Wouters, "FRET from single to multiplexed signaling events," *Biophys. Rev.*, vol. 9, no. 2, pp. 119–129, 2017.

[18] K. Austen *et al.*, "Extracellular rigidity sensing by talin isoform-specific mechanical linkages," *Nat. Cell Biol.*, vol. 17, no. 12, pp. 1597–1606, Dec. 2015.

[19] A. Kumar *et al.*, "Talin tension sensor reveals novel features of focal adhesion force transmission and mechanosensitivity," *J. Cell Biol.*, vol. 213, no. 3, pp. 371–383, May 2016.

[20] A. Piljic and C. Schultz, “Simultaneous Recording of Multiple Cellular Events by FRET,” *ACS Chem. Biol.*, vol. 3, no. 3, pp. 156–160, Mar. 2008.
[21] H. Chen, D. M. Cohen, D. M. Choudhury, N. Kioka, and S. W. Craig, “Spatial distribution and functional significance of activated vinculin in living cells,” *J. Cell Biol.*, vol. 169, no. 3, pp. 459–470, May 2005.
[22] B. Hochreiter, A. Pardo-Garcia, and J. Schmid, “Fluorescent Proteins as Genetically Encoded FRET Biosensors in Life Sciences,” *Sensors*, vol. 15, no. 10, pp. 26281–26314, Oct. 2015.
[23] C.-Y. Zhang, H.-C. Yeh, M. T. Kuroki, and T.-H. Wang, “Single-quantum-dot-based DNA nanosensor,” *Nat. Mater.*, vol. 4, no. 11, pp. 826–831, Nov. 2005.
[24] W. R. Algar, H. Kim, I. L. Medintz, and N. Hildebrandt, “Emerging non-traditional Förster resonance energy transfer configurations with semiconductor quantum dots: Investigations and applications,” *Coord. Chem. Rev.*, vol. 263–264, no. 1, pp. 65–85, Mar. 2014.
[25] J. Hu, M. Liu, and C. Zhang, “Construction of Tetrahedral DNA-Quantum Dot Nanostructure with the Integration of Multistep Förster Resonance Energy Transfer for Multiplex Enzymes Assay,” *ACS Nano*, vol. 13, no. 6, pp. 7191–7201, Jun. 2019.
[26] J. Guo *et al.*, “Conformational Details of Quantum Dot-DNA Resolved by Förster Resonance Energy Transfer Lifetime Nanoruler,” *ACS Nano*, vol. 13, no. 1, pp. 505–514, Jan. 2019.
[27] S. J. Ghilardi, M. S. Aronson, and A. E. Sgro, “Ventral stress fibers induce plasma membrane deformation in human fibroblasts,” *Mol. Biol. Cell*, vol. 32, no. 18, pp. 1707–1723, Aug. 2021.
[28] F. Saltel *et al.*, “New PI(4,5)P2- and membrane proximal integrin–binding motifs in the talin head control β3-integrin clustering,” *J. Cell Biol.*, vol. 187, no. 5, pp. 715–731, Nov. 2009.
[29] E. Goksoy *et al.*, “Structural Basis for the Autoinhibition of Talin in Regulating Integrin Activation,” *Mol. Cell*, vol. 31, no. 1, pp. 124–133, Jul. 2008.
[30] H. Tachibana *et al.*, “The plasma membrane of focal adhesions has a high content of cholesterol and phosphatidylcholine with saturated acyl chains,” *J. Cell Sci.*, vol. 136, no. 16, Aug. 2023.
[31] A. R. Gingras *et al.*, “The structure of the C-terminal actin-binding domain of talin,” *EMBO J.*, vol. 27, no. 2, pp. 458–469, Jan. 2008.
[32] A. Coullomb *et al.*, “QuanTI-FRET: a framework for quantitative FRET measurements in living cells,” *Sci. Rep.*, vol. 10, no. 1, p. 6504, Apr. 2020.
[33] C. Würth, D. Geißler, and U. Resch-Genger, “Quantification of anisotropy-related uncertainties in relative photoluminescence quantum yield measurements of nanomaterials-semiconductor quantum dots and rods,” *Zeitschrift fur Phys. Chemie*, vol. 229, no. 1–2, pp. 153–165, 2015.
[34] I. Medintz and N. Hildebrandt, *FRET - Förster Resonance Energy Transfer*. Weinheim, Germany: Wiley-VCH Verlag GmbH & Co. KGaA, 2013.
[35] J. Jumper *et al.*, “Highly accurate protein structure prediction with AlphaFold,” *Nature*, vol. 596, no. 7873, pp. 583–589, Aug. 2021.
[36] M. Yao, B. T. Goult, H. Chen, P. Cong, M. P. Sheetz, and J. Yan, “Mechanical activation of vinculin binding to talin locks talin in an unfolded conformation,” *Sci. Rep.*, vol. 4, no. 1, p. 4610, May 2015.
[37] P. Atherton *et al.*, “Vinculin controls talin engagement with the actomyosin

machinery," *Nat. Commun.*, vol. 6, no. 1, p. 10038, Dec. 2015.
[38] A. W. M. Haining, M. von Essen, S. J. Attwood, V. P. Hytönen, and A. del Río Hernández, "All Subdomains of the Talin Rod Are Mechanically Vulnerable and May Contribute To Cellular Mechanosensing," *ACS Nano*, vol. 10, no. 7, pp. 6648–6658, Jul. 2016.
[39] L. Borges-Araújo, M. M. Domingues, A. Fedorov, N. C. Santos, M. N. Melo, and F. Fernandes, "Acyl-chain saturation regulates the order of phosphatidylinositol 4,5-bisphosphate nanodomains," *Commun. Chem.*, vol. 4, no. 1, p. 164, Nov. 2021.
[40] K. Susumu *et al.*, "Multifunctional compact zwitterionic ligands for preparing robust biocompatible semiconductor quantum dots and gold nanoparticles," *J. Am. Chem. Soc.*, vol. 133, no. 24, pp. 9480–9496, 2011.
[41] M. Collot *et al.*, "MemBright: A Family of Fluorescent Membrane Probes for Advanced Cellular Imaging and Neuroscience," *Cell Chem. Biol.*, vol. 26, no. 4, pp. 600-614.e7, Apr. 2019.
[42] C. Vigouroux, V. Henriot, and C. Le Clainche, "Talin dissociates from RIAM and associates to vinculin sequentially in response to the actomyosin force," *Nat. Commun.*, vol. 11, no. 1, pp. 1–11, 2020.
[43] C. Ciobanasu, B. Faivre, and C. Le Clainche, "Reconstituting actomyosin-dependent mechanosensitive protein complexes in vitro," *Nat. Protoc.*, vol. 10, no. 1, pp. 75–89, Jan. 2015.
[44] T. D. Pollard, "Chapter 22 Myosin Purification and Characterization," in *Methods in Cell Biology*, vol. 24, no. C, 1982, pp. 333–371.
[45] A. Weinberger *et al.*, "Gel-Assisted Formation of Giant Unilamellar Vesicles," *Biophys. J.*, vol. 105, no. 1, pp. 154–164, Jul. 2013.
[46] B. W. VanDerMeer, "Kappaphobia is the elephant in the fret room," *Methods Appl. Fluoresc.*, vol. 8, no. 3, p. 030401, Jul. 2020.